Shock loading on AlN ceramics: A large scale molecular dynamics study

Paulo S. Branicio [a,*], Aiichiro Nakano [b], Rajiv K. Kalia [b], Priya Vashishta [b]

[a] Institute of High Performance Computing, 1 Fusionopolis Way 16-16, Connexis, 138632, Singapore
[b] Collaboratory for Advanced Computing and Simulations, Departments of Chemical Engineering and Materials Science, Physics and Astronomy, and Computer Science, University of Southern California, Los Angeles, CA 90089, United States

ARTICLE INFO

ABSTRACT

The nanoscale structure of shock waves in high strength AlN ceramics is studied using molecular-dynamics simulations. Impacts using four independent crystallographic directions, with particle velocities in the range 0.8–4.0 km/s, reveal the generation of a well-defined two-wave structure, consisting of an elastic precursor followed by a wurtzite-to-rocksalt structural transformation wave (STW). Impacts with particle velocities below 0.8 km/s or above 4.0 km/s generate single elastic or single overdriven shock waves, respectively. The latter propagates faster than the longitudinal sound velocity along the impact direction. The structure of the STW exhibits a strong anisotropy with respect to the crystallographic directions. Results show distinct shock front features from a steady, sharp and well defined STW front for impact at the basal plane to a rough STW front with the formation of an intermediate metastable fivefold coordinated phase or the generation and propagation of dislocations from the shock front for impact at other directions. These results indicate that shock-induced damage in brittle materials can be highly intricate even in defect-free systems. Simulations show no deformation twinning or other well defined plastic wave as found in experiments on polycrystalline AlN suggesting that interfaces and defects strongly affect the materials response to shock loading.

1. Introduction

Molecular-dynamics (MD) simulations of shock waves have been performed for over three decades to test the validity of shock wave theories and to provide microscopic details of shock propagation (Holian, 1988; Holian et al., 1980; Holian and Straub, 1979). Early simulations were performed in simple solids and liquids to investigate the nature of shock waves such as the shock evolution and shear stress relaxation mechanisms. Later, they were used to describe complex phenomena such as multi-shock wave structures induced by polymorphic phase transitions (Robertson et al., 1991), and intricate energetic materials supporting chemically sustained shock waves (Brenner et al., 1993).

Large scale MD simulations of shock wave present a new dimension for the description of shock phenomena, narrowing the gap between experimental studies and microscopic models of shock phenomena. Using large scale simulations, plastic deformations on the shock front in metallic systems can finally be described in fine details along with the rich dynamic nanostructures left behind the shock interface (Holian and Lomdahl, 1998). Details of the shock propagation in metals along multiple crystallographic directions (Bringa et al., 2004; Germann et al., 2000, 2004), as well as the shear stress released by nucleation of complex dislocation structures (Tanguy et al., 2003), and induced structural phase transitions (Kadau et al.,

2002) can be described accurately. Large scale MD simulations were also employed successfully to describe the strength of nanocrystalline metals under shock (Bringa et al., 2005).

Recently, the interest in studying shock effects in high strength ceramics has increased because of potential application of these materials as coatings for improved light weight armor designs. The literature of experimental studies of these ceramics is extensive and includes shock experiments on a wide range of materials such as Al_2O_3, B_4C, SiC, Si_3N_4, and AlN (Dandekar, 1994; Dandekar et al., 1994; Gorelskii et al., 2000; Grady, 1994, 1998; Kanel et al., 2009; Kipp and Grady, 1994; Mashimo et al., 1999b; Rosenberg et al., 1991).

Due to intrinsic differences in physical and chemical properties there can be large differences between the shock behavior among different classes of solid materials, e.g. metals and ceramics. While the previously cited MD simulations of shock in metallic materials are instructive and provide a good framework to further investigations, MD simulations of shock in ceramics must be performed to describe the distinct features of shock loading in this class of materials. While MD simulations of projectile impact were previously employed to investigate the generation of damage and fracture in AlN ceramics (Branicio et al., 2006, 2008) there is still a lack in the understanding of the shock induced features in AlN and other ceramics. Shock loading experiments in AlN have shown the generation of a complex set of multiple wave structures including a plastic and a structural transformation wave (Mashimo et al., 1999b). However, it is not clear from a nanoscale and atomistic point of view, how a shock pulse is absorbed in AlN, how it generates different types of wave structures and how does that depend on the shock intensity. It is also not clear what are the effects of shock loading direction considering different crystallographic directions of a single AlN crystal and what are the effects of grain size and grain boundaries in the shock propagation and generation of plastic deformation.

In this work we aim to address some of these questions performing large MD simulations in a well defined and controlled shock loading environment using plane shocks in defect free single crystals of AlN. We employed a wide range of shock intensity from very weak shocks generating particle velocities $u_p \sim 100$ m/s, to very strong shocks with $u_p \sim 5$ km/s. The forces among atoms are calculated from a many-body interatomic potential validated by experimental results on lattice constants, elastic moduli, cohesive energy, and melting temperature (Vashishta et al., 2011). A more stringent validation of the potential is provided by the wurtzite-to-rocksalt structural phase transition in AlN. High-pressure experiments reveal that this transformation occurs at ~20 GPa (Mashimo et al., 1999a) which is close to the calculated value of 25 GPa. This potential has been used successfully to describe shock-induced damage and fracture in projectile impacts on AlN (Branicio et al., 2006, 2008). The same potential form has also been successfully applied to describe the mechanical behavior of similar ceramics such as SiC (Branicio, 2012; Branicio et al., 2010; Kikuchi et al., 2005; Rino et al., 2004; Tsuzuki et al., 2011) and Al_2O_3 (Zhang et al., 2007a,b, 2008).

2. Methods and simulation procedures

The simulated systems are AlN single crystal slabs of about $15 \times 15 \times 200$ nm^3 dimensions containing 4 million atoms. The long system dimension, along the z direction, is aligned with the impact direction to allow the shock waves to develop for at least 15 ps. Before impact, the crystalline structure of the target material is a defect-free wurtzite. In order to perform impact on different crystallographic orientations of the wurtzite crystal, the slab is oriented in such a way that the z-axis, chosen as the impact direction, is parallel to one of the low index orthogonal crystallographic directions: $[0\,0\,0\,1]$, $[1\,1\,\bar{2}\,0]$, and $[1\,0\,\bar{1}\,0]$. An additional oblique direction, with an irrational Miller index, is prepared to access the shock response of the system out of the low-index crystalline directions. It is prepared from a system initially with directions x, y, and z aligned with $[1\,0\,\bar{1}\,0]$, $[1\,1\,\bar{2}\,0]$, and $[0\,0\,0\,1]$, respectively, rotating the crystal clockwise by $62°$ on the z–x plane. Therefore, the oblique impact direction is perpendicular to the $[1\,1\,2\,0]$ direction and parallel to the $[0\,0\,0\,1]$–$[1\,0\,\bar{1}\,0]$ plane, making an angle of $62°$ with the $[0\,0\,0\,1]$ direction. To construct such an oblique system while keeping periodicity, and avoiding introducing new surfaces, a large 472-atom super cell is defined from within the rotated crystal in order to generate negligible residual stress. The calculated residual shear stress for the oblique supercell is less than 0.3 GPa and is orders of magnitude smaller than those generated during the shock simulations. All simulations are performed with periodic boundary conditions in the x and y directions and free surfaces along the z direction. The particle velocity, which here is the same as the impact velocity, is in the range of 0.2–5 km/s, and it accesses all shock wave regimes and induced shock pressures up to 150 GPa. The equations of motion are numerically integrated using the velocity-Verlet algorithm with a time step of 1.5 fs. For the range of impacts velocities investigated this time step is small enough to allow stable integration of the equations of motion for all atoms and the conservation of the energy during all simulations to at least the third meaningful digit. Simulations are performed with systems initially at $T = 10$ K and $T = 300$ K to evaluate the effect of temperature in the shock Hugoniot. After the systems are initially equilibrated shock simulations are performed in the NVE ensemble. The planar impact simulations are performed in the reversed geometry with the system target hitting the piston at a fixed position with a chosen impact velocity. The piston is a hard wall, which instantly bounces any particle hitting its surface by inverting the component of the momentum perpendicular to the hard wall. Shock profile of properties is calculated along the system in the impact z direction. Bins 5 Å wide are used to average local quantities and quantify the shock profile which here includes the particle velocity, stresses, internal energy, displacement in the xy plane, and density. Particular care is taken in the calculation of the latter. The usual method of direct average of atoms on bins is replaced by the average of the inverse atomic Voronoi polyhedral volumes. Such volumes calculated from the Voronoi tessellation (Brostow et al., 1978; Finney, 1979; Tanemura et al.,

1983) defined by the local crystalline topology give the space occupied by the atoms in the crystal and its inverse, when averaged locally, gives an accurate measure of the local density (Branicio and Srolovitz, 2009). Since the shock induced densities calculated are very accurate we use them in the Hugoniot equation, $u_p/u_s = 1 - \rho_0/\rho$, to evaluate shock wave velocities, avoiding the elusive task of defining the position and tracking the propagation of shock wave fronts directly.

3. Results and discussions

We have found three regimes for the shock response, which agree well with experiments. The shock Hugoniot curves from our simulations at $T = 10$ K and $T = 300$ K are shown in Fig. 1(a) and (b). The calculated shock velocities as a function of particle velocities are compared with the experimental result of Mashimo et al. (1999a). Experimental data is shown with a linear fitted curve, following the original publication, while the data from this work have lines as a guide to the eye. For particle velocities below $u_p = 0.8$ km/s the simulation shows the presence of a solitary elastic shock wave propagating with constant velocity. Experimentally, at low particle velocities up to $u_p = 0.6$ km/s only an elastic wave is generated, which is in excellent agreement with our simulation result. However, between $u_p = 0.6$ km/s and $u_p = 1$ km/s experiments show an intermediate shock wave arguably induced by plastic deformations in the sample (Mashimo et al., 1999a). In our simulations, which assume defect free single crystals, the results show no well-defined plastic wave. As will be discussed later, results indicate that the only sign of plasticity present in the simulations is in the form of generation and propagation of few partial dislocations from the shock front for impact on the oblique direction, which however does not affect significantly the shock profiles. The simulation results in Fig. 1 indicate that above $u_p = 0.8$ km/s a structural phase transition shock wave develops inside the system and propagates at higher speeds for higher u_p. Experimentally, the transformation wave is observed for particle velocities above $u_p = 1$ km/s and propagates with higher speeds for stronger shock loads. Despite the differences in system geometry and crystal structures, the simulation results agree reasonably well with the experimental Hugoniot
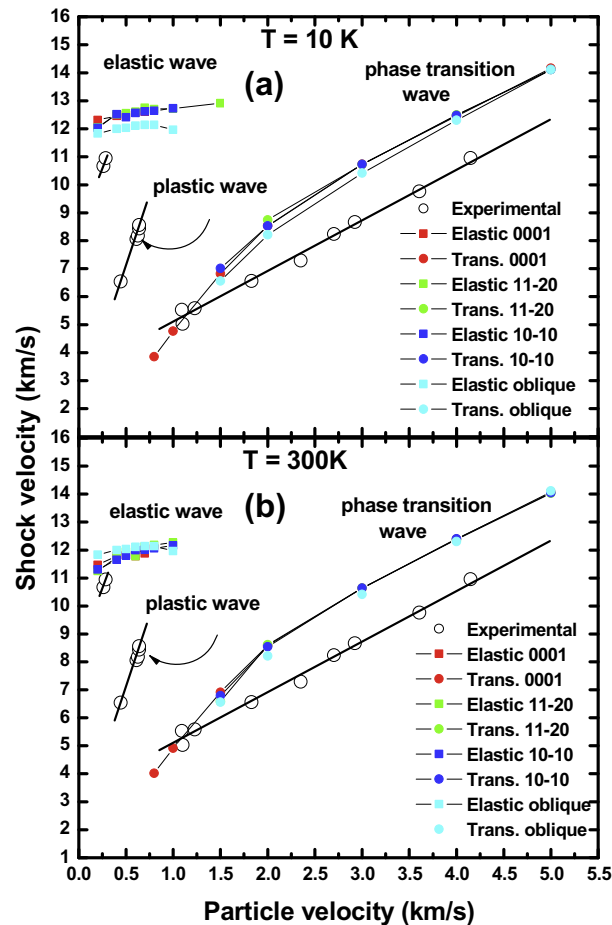
Fig. 1. AlN shock Hugoniot at $T = 10$ K and $T = 300$ K for several crystallographic directions. MD and experimental data are shown in filled symbols and open circles, respectively. MD results are calculated for a single crystal with $[0001]$, $[11\bar{2}0]$, $[10\bar{1}0]$ and oblique (see text) directions aligned with the shock direction while the experimental data is obtained using a polycrystalline sample.

curves. For particle velocities above u_p = 4.0 km/s, the structural phase transition wave overlaps with the elastic wave, forming a single overdriven wave. As can be observed the results indicate that no plastic wave is induced by the uniaxial compression before the structural transformation takes place. As can be seen comparing the shock Hugoniot displayed in Fig. 1(a) and (b) there are no significant effect of temperature. For all the following analysis we use the results of the simulations performed at T = 10 K in order to minimize the thermal effect over the structural analysis and he calculation of shock profiles.

One should note that we use a direct method to evaluate the shock Hugoniot, which is suitable to investigate induced shock dynamics mechanisms such as structural phase transformation shock fronts and possible plastic waves. However, other indirect methods such as that proposed by Erpenbeck (1992) and Rice et al. (1996), offer a convenient and computationally efficient procedure to evaluate the Shock Hugoniot states behind the shock fronts, which is particularly indicated if one intend to use computationally intensive description of the interatomic forces such as within the Density Functional Theory (Chantawansri et al., 2012; Chen et al., 2012).

We have quantified the shock waves in different crystallographic directions by calculating the profiles of several physical quantities in the system along the shock propagation, see Section 2 for details. Fig. 2(a)–(e) show shock profiles for the [0 0 0 1] direction with u_p = 1 km/s calculated after 14.7 ps of the initial impact. Abrupt changes in particle velocity are a clear signature of the presence of shock waves. Fig. 2(a) shows that the particle velocity's suddenly change to ~730 m/s at the elastic wave front and maintains that value until the arrival of the transformation wave when it reaches quickly 1 km/s. Other quantities, such as density, stress, energy and temperature also change abruptly in the shock wave front. Fig. 2(b) shows the profile of local density and quantifies the compression of the system. At the elastic front, the density increases mildly from 3.26 g/cm³ to 3.46 g/cm³. However, at the transformation front the density quickly reaches 4.1 g/cm³, which is about 26% higher than the initial value in the relaxed structure. A useful quantity to distinguish elastic waves from
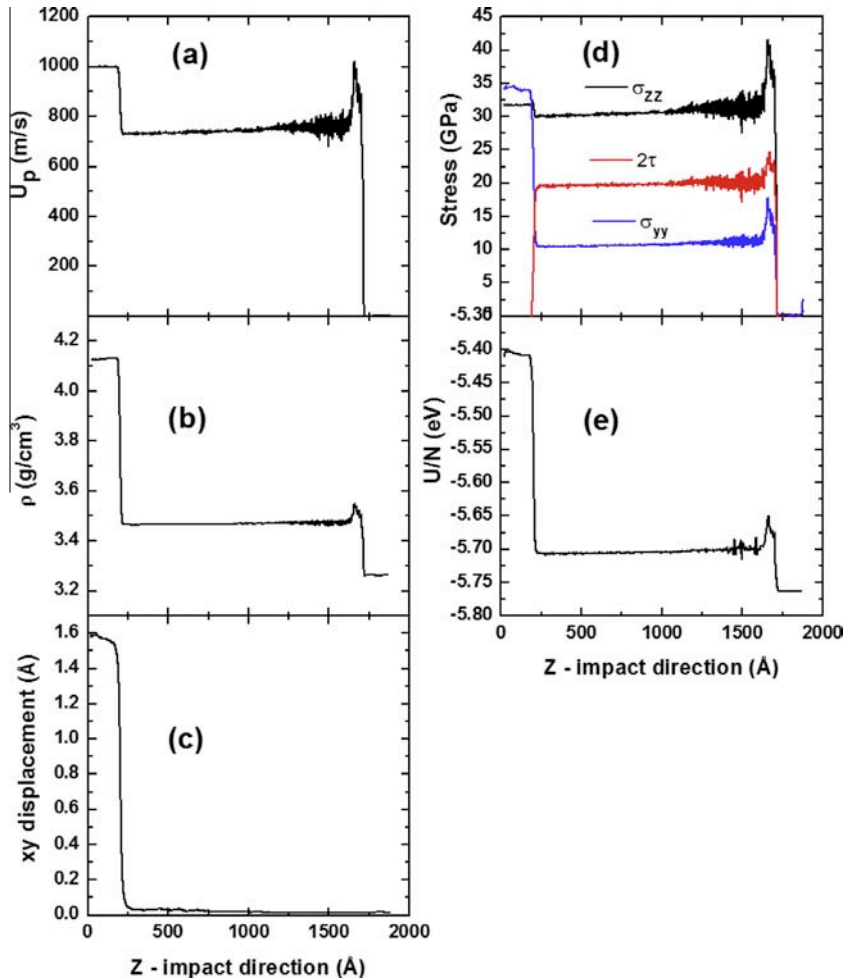
Fig. 2. Shock profiles for impact at T = 10 K, with u_p = 1 km/s, on AlN [0 0 0 1] at 14.7 ps after initial impact. (a) Particle velocities averaged locally along the impact direction; (b) density profile; (c) average displacement of particles on the xy plane perpendicular to the shock direction; (d) stress profile showing the longitudinal and shear components; (e) changes in the internal energy during the elastic and transformation wave propagation.

transformation waves is the average displacement perpendicular to the impact. Fig. 2(c) shows the average displacement of the particles in the xy plane, transverse to the shock direction, indicating accurately the threshold for the transformation. At the transformation front, the average atomic displacement is ∼1.5 Å. As shown in Fig. 2(c), the xy displacement occurs very quickly in the shock front and is stable in the transformed region. Stress and energy profiles in Fig. 2(d) and (e) show the release of the large shear stress created by the elastic wave at the transformation front and the internal energy changes during the elastic and transformation waves.

For the [0 0 0 1] direction the transformation front is sharp and stable and no intermediate region exists. Fig. 3(a)–(f) show the structure of the transformation wave for the [0 0 0 1] direction. Fig. 3(a) and (b) show the shock profiles at particle velocity u_p = 1 km/s. In Fig. 3(a) the density profile shows an elastic wave (yellow with ∼3.46 g/cm^3) with a sharp front propagating to the right into the uncompressed material (grey with 3.26 g/cm^3). A slower transformation wave (red with 4.1 g/cm^3) runs behind the elastic wave and drives the system to the rocksalt phase which has a density 26% higher than that of the original wurtzite as discussed. Atoms are color coded by their coordination number in Fig. 3(b)–(f), which here are defined as the number of neighbors up to 2.5 Å. Grey, red and yellow indicate atoms in the wurtzite phase (coordination 4), rocksalt phase (coordination 6) or compressed wurtzite phase and grain boundaries (coordination 5), respectively. Fig. 3(b) highlight the atomic structure of the transformation wave, indicating that for u_p = 1 km/s the transformation takes place by a grain-growth mechanism, i.e. the transformation wave propagates along the impact direction by growing the original grains nucleated at the impact surface. That is a clear indication of heterogeneous nucleation of the rock salt phase.

Fig. 3(c) shows details of the rocksalt grain structure on a plane at 5 Å from the impact surface. Each grain corresponds to a rocksalt nucleation point. It can be seen that grains have different sizes and, besides fluctuations, they are aligned in three main directions. These directions are crystallographically equivalent and originate from the hexagonal symmetry of the wurtzite crystal. That suggests a well-defined path for the transformation to the rocksalt phase. The different paths defined by the atomic transformation mechanisms to the rocksalt phase were described by Shimojo et al. (2004). For impacts along the [0 0 0 1] direction they describe accurately the transformation observed in the simulations, even though no intermediate stable phase is observed. For u_p up to 2 km/s, the final temperature is below 1,000 K and the healing of the grains is limited. Grain healing in ceramics, in contrast with metals, is limited until the system is close to the high particle velocity and high temperature melting limit; see Fig. 3(f). Increasing the impact velocity and particle velocity changes the propagation and structure of the transformation wave. For u_p = 1 km/s the transformation front is sharp and stable and the mechanism of propagation is based on grain growth of the grains nucleated at the face; see Fig 3(b).

For u_p = 2 km/s, the propagation front is rough and several grains are nucleated as the transformation front propagates; see Fig. 3(d). At u_p = 5 km/s the transformation front becomes sharp again and the grain growth cannot follow the fast propagation of the transformation front. At that point a high density of new rocksalt grains is nucleated in the front region. These grains heal behind the front into larger energetically favored grains; see Fig 3(f). As can be noted the grain boundaries shown in Fig. 3(f) are not well defined, as those shown in Fig. 3(c), because temperature fluctuations induce fluctuations in the
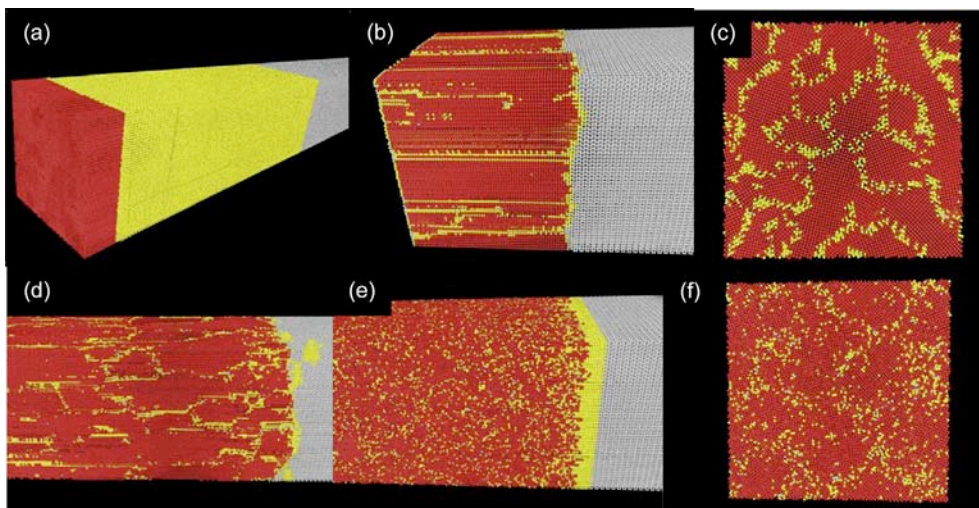
Fig. 3. Shock structures due to impact at T = 10 K, in [0 0 0 1] direction. (a), (b), (d) and (e) show waves propagating to the right direction. (a) and (b) Shock wave profiles at u_p = 1 km/s. (a) Density profile showing uncompressed material (3.26 g/cm^3) in grey, elastically compressed region in yellow (3.46 g/cm^3) and transformed region in red (4.1 g/cm^3). (b) Structure of transformed atoms illustrating grain growth during transformation propagation. Atoms in (b)–(f) are color coded by their coordination number, defined here as the number of neighbors up to 2.5 Å. Grey indicates atoms with 4 neighbors in the original wurtzite (WZ) crystal. Red indicates atoms with 6 neighbors in the rocksalt (RS) transformed crystal. Yellow indicates atoms with 5 neighbors in the compressed region of the shock front or in RS grain boundaries. (c) Illustration of front face of system impacted at u_p = 1 km/s. (d) Transformation at u_p = 2 km/s; (e) transformation at u_p = 5 km/s; (f) Illustration of front face of system impacted at u_p = 5 km/s. (For interpretation of the references to color in this figure legend, the reader is referred to the web version of this article.)

calculated coordination number. Therefore from $u_p = 1$ km/s to $u_p = 5$ km/s we can see a gradual change in the transformation dynamics from heterogeneous nucleation of grains, at the impact surface and propagation by grain growth to heterogeneous nucleation of grains at the propagating shock front. One should note that the systems cross sections used in the simulations can accommodate several grains across and therefore do not constrain or affect the nucleation of the rocksalt phase. To confirm this we simulate a system with a cross section twice as long in each direction, i.e., with a cross section area four times larger. The results indicated a similar grain size distribution and density of grains per area.

Shocks in AlN ceramics present a strong anisotropy of the transformation wave for different crystallographic directions. For all directions investigated the calculated Hugoniot curves indicates the presence of similar elastic and transformation waves for values of u_p in the range from 0.8 km/s to 5 km/s. However, the transformation wave is sharp only for impacts on the basal [0001] direction. For shocks in the [11$\bar{2}$0] direction, the propagation of the transformation wave starts with a sharp front similar to that for the [0001] direction. After propagating for a few ps the front becomes rough and an intermediate phase with 5-fold coordination grows from the transformation front into the compressed region ahead of
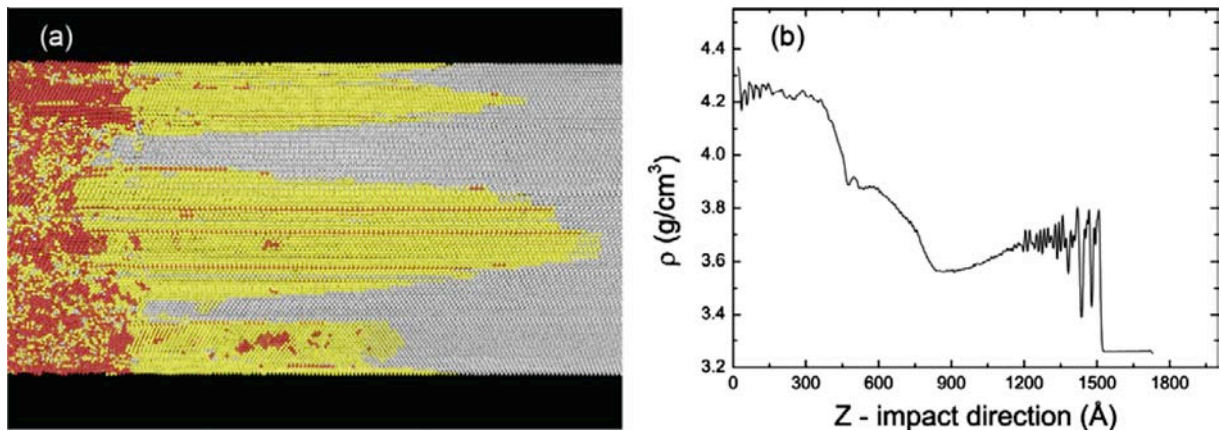
Fig. 4. Shock structure and profile due to impact in [11$\bar{2}$0] direction at $u_p = 2$ km/s and $T = 10$ K. (a) Shock atomic structure with atoms colored by their coordination number as in Fig. 3(b)–(f); (b) corresponding density profile.
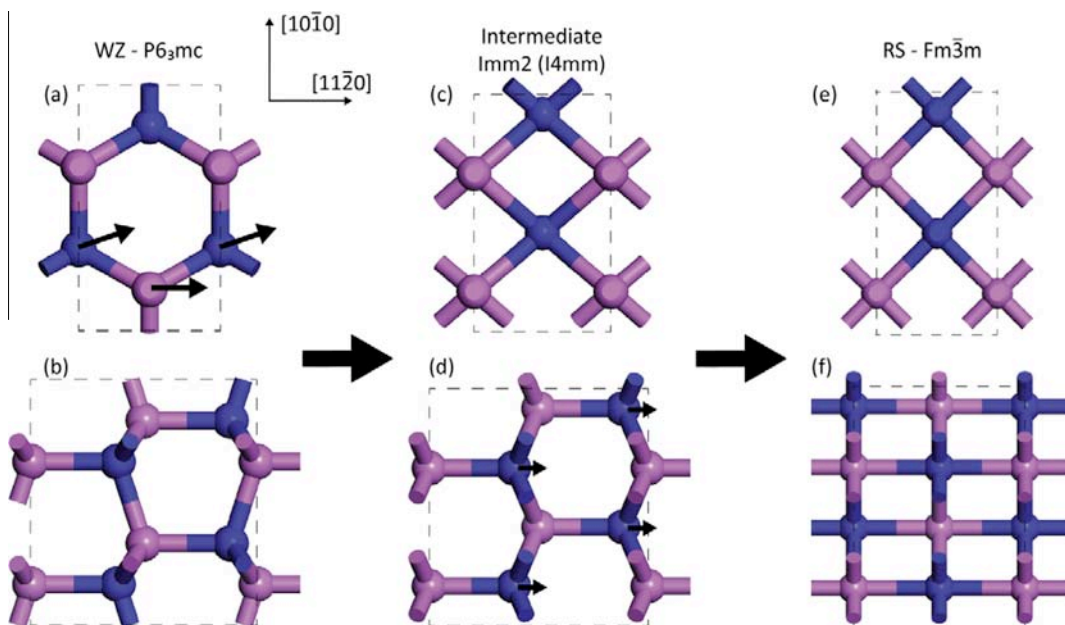
Fig. 5. Mechanism of the WZ-to-RS structural phase transformation for impact in [11$\bar{2}$0] direction. The magenta and blue spheres show the atomic positions of the Al and N atoms, respectively. The small arrows displayed in (a) and (d) indicate the directions to which internal coordinates are shifted. (a) and (b) show AlN in the initial WZ (P6$_3$mc) structure with views from the [0001] and [11$\bar{2}$0] directions. (c) and (d) shows the intermediate 5-coordinated structure which was highlighted in Fig. 4(a). In the simulations the symmetry of the structure found is Imm2, while ideally, it should be I4 mm, if all bonds lengths were identical. (e) and (f) shows the final RS (Fm$\bar{3}$m) structure. (For interpretation of the references to color in this figure legend, the reader is referred to the web version of this article.)

the transformation wave. Fig. 4(a) shows the intermediate 5 coordinated region growing ahead of the transformation developing arrow like shapes for u_p = 2 km/s. Because of the shape of the intermediate region it makes the roughness of the transformation front reach hundreds of nanometers, during the simulation time. However, much longer simulations, with correspondingly much larger systems, would be required to investigate the equilibrium roughness of the transformation wave. Since the roughness introduced in the transformation shock front implies changes in the particle velocity and density, the shock profile along the shock direction becomes a ramp; see Fig. 4(b).

It is worth noting that this intermediate phase is of different character than the HS phase described by Shimojo et al. (2004) which is generated when the basal (0 0 0 1) plane of the wurtzite becomes flat. In the simulations instead, the intermediate phase is generated by shifts in (0 0 0 1) basal planes, preceding the transformation to the rocksalt and is independent from all transformation paths described previously. The complete transformation path including this intermediate phase is illustrated in Fig. 5. The intermediate (metastable) phase for impact on the [1 1 $\bar{2}$ 0] direction is found to be an orthorhombic pyramidal structure (space group Imm2). The phase found is however strained and it would transform into a ditetragonal pyramidal (space group I4 mm) in a hydrostatic state, generating a single bond length for all 5 bonds of Al and N atoms. This transformation path, although similar to the ones described by Shimojo et al. (2004), is novel and was not found in the wurtzite-to-rocksalt pressure induced transformation investigated for cadmium selenide. The transformation path found for AlN is also independent from those found by Sharma and Gupta (1998) and Knudson et al. (1999) for shocked wurtzite crystals (CdS), suggesting the presence of a face centered orthorhombic and face centered tetragonal phases, respectively. An independent transformation path for the WZ to RS transformation under pressure involving homogenous orthorhombic shear-strain deformation was also proposed by Limpijumnong and Lambrecht (2001a,b) for GaN and MgO. This mechanism is also different than the one observed here for AlN. Theses previous investigations demonstrated that the actual path for the pressure or shock induced WZ-to-RS transformation may be different for different materials and shock loading directions. It should be noted that the prediction of this intermediate metastable phase for impacts in the [1 1 $\bar{2}$ 0] direction points to distinct transformation paths to the rocksalt phase as a function of impact direction.

Results from shock in the [1 0 $\bar{1}$ 0] direction indicate that a similar intermediate region runs ahead of the transformation front. However, because of the crystallographic direction alignment, instead of propagating directly into the impact direction it propagates diagonally, in the [1 1 $\bar{2}$ 0] direction – see Fig. 6(a) – following the same transformation path illustrated in Fig. 5.
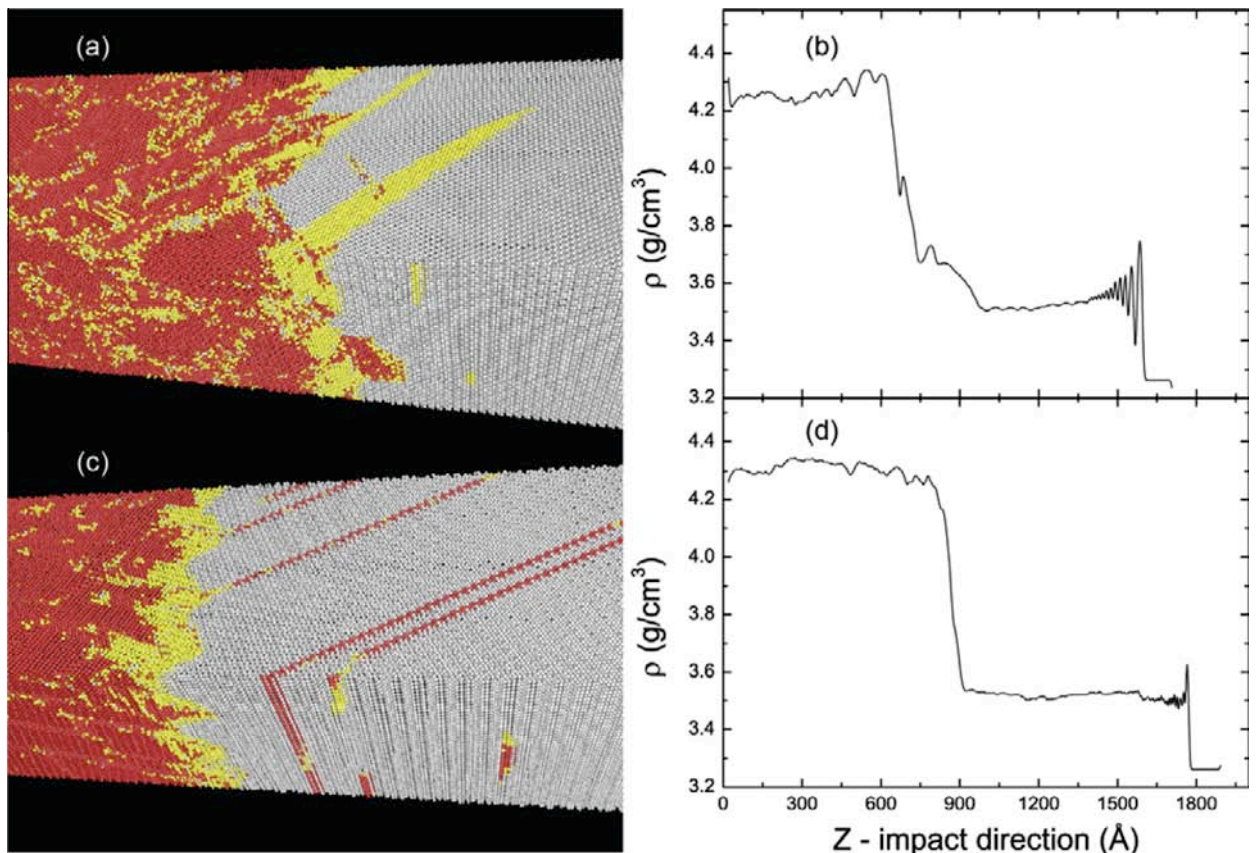
Fig. 6. Shock structure and profile at T = 10 K, due to impact in the [1 0 $\bar{1}$ 0] and oblique directions at u_p = 2 km/s. (a) and (c) Shock atomic structure for impact in [1 0 $\bar{1}$ 0] and oblique directions with atoms colored by coordination number as in Fig. 3(b)–(f); (b) and (d) corresponding density profiles.

Similar to the impact in the $[11\bar{2}0]$ direction, the shock profile shows that the shock front loses the sharpness and becomes rough, see Fig. 6(b). In the oblique direction, results show a sharp transformation front. However, microscopic analysis indicates that ahead of the transformation front a few partial dislocations are nucleated and glide in the compressed region on the (0001) plane; see Fig. 6(c). While the effect of the dislocation motion can be observed in the xy displacement profile, because of the relative plane sliding, and also mildly in the density profile, see small bump at $\sim$1655 Å in Fig. 6(d), these dislocations have no noticeable effect on the particle velocity, stress, or internal energy profiles. Therefore, the transformation wave front remains sharp and we do not consider that the propagation of the dislocations constitute a typical plastic wave as that observed experimentally (Mashimo et al., 1999b).

It is worthwhile to note that the simulations do not show the presence of any plastic wave and no signs of deformation twinning (DT). In hexagonal crystals, such as the wurtzite structure of the AlN, glide planes are limited and plastic deformation usually occurs by twinning, making it a major source of induced plasticity in materials such as Mg, ZnO, and Al_3O_4 (Barrett et al., 2012a,b; Kuksin and Yanilkin, 2012; Mashimo et al., 2011; Yan et al., 2005; Zhang et al., 2007a,b, 2008). Grain boundaries and defects were shown to play a major role in initiating deformation twinning (Barrett et al., 2012a,b; Kuksin and Yanilkin, 2012). However, under intense shock conditions twins were shown to be generated and propagate in multiple modes in simulations of defect free single crystal Al_3O_4 (Zhang et al., 2007a,b, 2008). The simulations results for AlN point out for a rather unusual behavior of AlN among hexagonal crystal materials indicating that its twinning energy barrier is very high and favors the release of shock shear stress by structural transformation rather than by twinning. As reported previously (Bernstein and Tadmor, 2004; Van Swygenhoven et al., 2004; Weinberger and Cai, 2012) the generalized stacking fault energy, and in particular the ratio of the unstable to stable stacking fault energy, provide key ingredients to understand and describe the onset and development of plastic deformation in materials, e.g. dislocation nucleation and motion and activation of twinning. The predicted energy barriers for plastic deformations predicted by the current interatomic potential were reported previously (Branicio et al., 2008). The calculated generalized stacking fault curve reasonably agreed with DFT predictions. The value of the unstable stacking fault energy was predicted to be 133 meV/Å^2 compared to 147 meV/Å^2 from DFT while the unstable twinning energy was predicted to be 130 meV/Å^2 compared to 152 meV/Å^2 from DFT. The results are also corroborated by a study of Yan et al. (2005) which demonstrated that the $[1\bar{1}00]/(1\bar{1}02)$ twin boundary energy in AlN is 0.109 J/m^2, which is higher than that in GaN and InN, and more than double the one in ZnO, where twinning is often observed. Therefore the absence of DT in the simulations of AlN in face of the experimental evidence of it and the reasonably accurate description of the energy barriers by the potential suggest that in fact grain boundaries and defects play a key role in the shock response of AlN. One should also note that while plausible the absence of DT in the simulations may also be an effect of the relatively short simulation times involved.

4. Conclusions

In summary, we have performed large scale planar shock-wave simulations on AlN ceramics. We have found and described three shock response regimes. Depending on the particle velocity, the shock wave structure is composed of a single elastic wave, a transformation wave preceded by a faster elastic component, or a single overdriven wave faster than the longitudinal sound velocity along the impact direction. The crossover between regimes are calculated to be at u_p = 0.8 km/s and u_p = 4.0 km/s, in good agreement with experiments. We have found a strong anisotropy for the transformation structure with crystallographic direction. For impact in the basal $[0001]$ direction, the transformation front is sharp and the shock profile is well defined. For shocks in the $[11\bar{2}0]$ and $[10\bar{1}0]$ directions, an intermediate metastable region with 5-fold coordinated atoms grows ahead of the transformation front making the transformation front roughness increase significantly to hundred nanometers. For shocks in the oblique direction, dislocations are nucleated and propagate in the compressed region ahead of the transformation. The results show that the shock response of high strength ceramics can be very complex even in single crystalline defect-free systems. It would be interesting to check these simulation predictions with shock experiments on single crystalline AlN ceramics. With the shock response of defect free single crystalline samples of different crystallographic directions established the natural follow up is to perform simulations on polycrystalline systems to clarify the effects of interfaces and defects on the induced shock damage.

Acknowledgments

References

Barrett, C.D., El Kadiri, H., Tschopp, M.A., 2012a. Breakdown of the Schmid law in homogeneous and heterogeneous nucleation events of slip and twinning in magnesium. Journal of the Mechanics and Physics of Solids 60, 2084–2099.
Barrett, C.D., Tschopp, M.A., El Kadiri, H., 2012b. Automated analysis of twins in hexagonal close-packed metals using molecular dynamics. Scripta Materialia 66, 666–669.
Bernstein, N., Tadmor, E.B., 2004. Tight-binding calculations of stacking energies and twinnability in fcc metals. Physical Review B 69, 094116.
Branicio, P.S., Srolovitz, D.J., 2009. Local stress calculation in simulations of multicomponent systems. Journal of Computational Physics 228, 8467–8479.

Branicio, P.S., Kalia, R.K., Nakano, A., Vashishta, P., 2006. Shock-induced structural phase transition, plasticity, and brittle cracks in aluminum nitride ceramic. Physical Review Letters 96, 065502.

Branicio, P.S., Kalia, R.K., Nakano, A., Vashishta, P., Shimojo, F., Rino, J.P., 2008. Atomistic damage mechanisms during hypervelocity projectile impact on AlN: a large-scale parallel molecular dynamics simulation study. Journal of the Mechanics and Physics of Solids 56, 1955–1988.

Branicio, P.S., Kalia, R.K., Nakano, A., Vashishta, P., 2010. Nanoductility induced brittle fracture in shocked high performance ceramics. Applied Physics Letters 97, 111903.

Branicio, P.S., 2012. Atomistic mechanisms in silicon carbide nanostructures. Journal of Computational and Theoretical Nanoscience 9, 1870.

Brenner, D.W., Robertson, D.H., Elert, M.L., White, C.T., 1993. Detonations at nanometer resolution using molecular-dynamics. Physical Review Letters 70, 2174–2177.

Bringa, E.M., Cazamias, J.U., Erhart, P., Stolken, J., Tanushev, N., Wirth, B.D., Rudd, R.E., Caturla, M.J., 2004. Atomistic shock Hugoniot simulation of single-crystal copper. Journal of Applied Physics 96, 3793–3799.

Bringa, E.M., Caro, A., Wang, Y.M., Victoria, M., McNaney, J.M., Remington, B.A., Smith, R.F., Torralva, B.R., Van Swygenhoven, H., 2005. Ultrahigh strength in nanocrystalline materials under shock loading. Science 309, 1838–1841.

Brostow, W., Dussault, J.P., Fox, B.L., 1978. Construction of Voronoi polyhedra. Journal of Computational Physics 29, 81–92.

Chantawansri, T.L., Sirk, T.W., Byrd, E.F.C., Andzelm, J.W., Rice, B.M., 2012. Shock Hugoniot calculations of polymers using quantum mechanics and molecular dynamics. Journal of Chemical Physics 137, 204901.

Chen, G.Y., Jiang, X.X., Cheng, X.L., Zhang, H., 2012. Phase transition and chemical decomposition of shocked CO–N-2 mixture. Journal of Chemical Physics 137, 054504.

Dandekar, D.P., Abbate, A., Frankel, J., 1994. Equation of state of aluminum nitride and its shock response. Journal of Applied Physics 76, 4077.

Dandekar, D.P., 1994. Shear strengths of aluminum nitride and titanium diboride under plane shock-wave compression. Journal de Physique IV 4, 379–384.

Erpenbeck, J.J., 1992. Molecular-dynamics of detonation. 1: Equation of state and Hugoniot curve for a simple reactive fluid. Physical Review A 46, 6406–6416.

Finney, J.L., 1979. Procedure for the construction of Voronoi polyhedra. Journal of Computational Physics 32, 137–143.

Germann, T.C., Holian, B.L., Lomdahl, P.S., Ravelo, R., 2000. Orientation dependence in molecular dynamics simulations of shocked single crystals. Physical Review Letters 84, 5351–5354.

Germann, T.C., Tanguy, D., Holian, B.L., Lomdahl, P.S., Mareschal, M., Ravelo, R., 2004. Dislocation structure behind a shock front in Fcc perfect crystals: atomistic simulation results. Metallurgical and Materials Transactions A-Physical Metallurgy and Materials Science 35A, 2609–2615.

Gorelskii, V.A., Zelepugin, S.A., Tolkachev, V.F., 2000. Experimental and numerical study of ceramics destruction by high-velocity impact. Chemical Physics Reports 18, 2211–2217.

Grady, D.E., 1994. Shock-wave strength properties of boron-carbide and silicon-carbide. Journal de Physique IV 4, 385.

Grady, D.E., 1998. Shock-wave compression of brittle solids. Mechanics of Materials 29, 181–203.

Holian, B.L., Lomdahl, P.S., 1998. Plasticity induced by shock waves in nonequilibrium molecular-dynamics simulations. Science 280, 2085–2088.

Holian, B.L., Straub, G.K., 1979. Molecular-dynamics of shock-waves in 3-dimensional solids – transition from nonsteady to steady waves in perfect crystals and implications for the Rankine–Hugoniot conditions. Physical Review Letters 43, 1598–1600.

Holian, B.L., Hoover, W.G., Moran, B., Straub, G.K., 1980. Shock-wave structure via non-equilibrium molecular-dynamics and Navier–Stokes continuum mechanics. Physical Review A 22, 2798–2808.

Holian, B.L., 1988. Modeling shock-wave deformation via molecular-dynamics. Physical Review A 37, 2562–2568.

Kadau, K., Germann, T.C., Lomdahl, P.S., Holian, B.L., 2002. Microscopic view of structural phase transitions induced by shock waves. Science 296, 1681–1684.

Kanel, G.I., Zaretsky, E.B., Rajendran, A.M., Razorenov, S.V., Savinykh, A.S., Paris, V., 2009. Search for conditions of compressive fracture of hard brittle ceramics at impact loading. International Journal of Plasticity 25, 649–670.

Kikuchi, H., Kalia, R.K., Nakano, A., Vashishta, P., Branicio, P.S., Shimojo, F., 2005. Brittle dynamic fracture of crystalline cubic silicon carbide (3C–SiC) via molecular dynamics simulation. Journal of Applied Physics 98, 103524.

Kipp, M.E., Grady, D.E., 1994. Shock phase-transformation and release properties of aluminum nitride. Journal de Physique IV 4, 249.

Knudson, M.D., Gupta, Y.M., Kunz, A.B., 1999. Transformation mechanism for the pressure-induced phase transition in shocked CdS. Physical Review B 59, 11704.

Kuksin, A.Y., Yanilkin, A.V., 2012. Formation of twins in sapphire under shock wave loading: atomistic simulations. Journal of Applied Physics 111, 033513.

Limpijumnong, S., Lambrecht, W.R.L., 2001a. Homogeneous strain deformation path for the wurtzite to rocksalt high-pressure phase transition in GaN. Physical Review Letters 86, 91.

Limpijumnong, S., Lambrecht, W.R.L., 2001b. Theoretical study of the relative stability of wurtzite and rocksalt phases in MgO and GaN. Physical Review B 63, 104103.

Mashimo, T., Uchino, M., Nakamura, A., Kobayashi, T., Takasawa, E., Sekine, T., Noguchi, Y., Hikosaka, H., Fukuoka, K., Syono, Y., 1999a. Yield properties, phase transition, and equation of state of aluminum nitride (AlN) under shock compression up to 150 GPa. Journal of Applied Physics 86, 6710–6716.

Mashimo, T., Uchino, M., Nakamura, A., Kobayashi, T., Takasawa, E., Sekine, T., Noguchi, Y., Hikosaka, H., Fukuoka, K., Syono, Y., 1999b. Yield properties, phase transition, and equation of state of aluminum nitride (AlN) under shock compression up to 150 GPa. Journal of Applied Physics 86, 6710.

Mashimo, T., Omurzak, E., Chen, L.L., Inoue, R., Kawai, C., 2011. Effect of shock compression on wurtzite-type ZnMgS crystals. Journal of Applied Physics 109, 023514.

Rice, B.M., Mattson, W., Grosh, J., Trevino, S.F., 1996. Molecular-dynamics study of detonation. 1: A comparison with hydrodynamic predictions. Physical Review E 53, 611–622.

Rino, J.P., Ebbsjo, I., Branicio, P.S., Kalia, R.K., Nakano, A., Shimojo, F., Vashishta, P., 2004. Short- and intermediate-range structural correlations in amorphous silicon carbide: a molecular dynamics study. Physical Review B 70, 045207.

Robertson, D.H., Brenner, D.W., White, C.T., 1991. Split shock-waves from molecular-dynamics. Physical Review Letters 67, 3132–3135.

Rosenberg, Z., Brar, N.S., Bless, S.J., 1991. Dynamic high-pressure properties of AlN ceramic as determined by flyer plate impact. Journal of Applied Physics 70, 167.

Sharma, S.M., Gupta, Y.M., 1998. Wurtzite-to-rocksalt structural transformation in cadmium sulphide shocked along the alpha axis. Physical Review B 58, R5964.

Shimojo, F., Kodiyalam, S., Ebbsjo, I., Kalia, R.K., Nakano, A., Vashishta, P., 2004. Atomistic mechanisms for wurtzite-to-rocksalt structural transformation in cadmium selenide under pressure. Physical Review B 70, 184111.

Tanemura, M., Ogawa, T., Ogita, N., 1983. A new algorithm for 3-dimensional Voronoi tessellation. Journal of Computational Physics 51, 191–207.

Tanguy, D., Mareschal, M., Lomdahl, P.S., Germann, T.C., Holian, B.L., Ravelo, R., 2003. Dislocation nucleation induced by a shock wave in a perfect crystal: molecular dynamics simulations and elastic calculations. Physical Review B 68, 144111.

Tsuzuki, H., Rino, J.P., Branicio, P.S., 2011. Dynamic behaviour of silicon carbide nanowires under high and extreme strain rates: a molecular dynamics study. Journal of Physics D-Applied Physics 44, 055405.

Van Swygenhoven, H., Derlet, P.M., Froseth, A.G., 2004. Stacking fault energies and slip in nanocrystalline metals. Nature Materials 3, 399–403.

Vashishta, P., Kalia, R.K., Nakano, A., Rino, J.P., Simulations, C.A.C., 2011. Interaction potential for aluminum nitride: a molecular dynamics study of mechanical and thermal properties of crystalline and amorphous aluminum nitride. Journal of Applied Physics 109, 033514.

Weinberger, C.R., Cai, W., 2012. Plasticity of metal nanowires. Journal of Materials Chemistry 22, 3277–3292.

Yan, Y.F., Al-Jassim, M.M., Chisholm, M.F., Boatner, L.A., Pennycook, S.J., Oxley, M., 2005. [1(1)$\bar{0}\bar{0}$]/(1$\bar{1}$02) twin boundaries in wurtzite ZnO and group-III-nitrides. Physical Review B 71, 041309.

Zhang, C., Kalia, R.K., Nakano, A., Vashishta, P., 2007a. Fracture initiation mechanisms in alpha-alumina under hypervelocity impact. Applied Physics Letters 91, 121911.

Zhang, C., Kalia, R.K., Nakano, A., Vashishta, P., 2007b. Hypervelocity impact induced deformation modes in alpha-alumina. Applied Physics Letters 91, 071906.

Zhang, C., Kalia, R.K., Nakano, A., Vashishta, P., Branicio, P.S., 2008. Deformation mechanisms and damage in alpha-alumina under hypervelocity impact loading. Journal of Applied Physics 103, 083508.